

Efficient modelling of droplet dynamics on complex surfaces

This content has been downloaded from IOPscience. Please scroll down to see the full text.

2016 J. Phys.: Condens. Matter 28 085101

(<http://iopscience.iop.org/0953-8984/28/8/085101>)

View [the table of contents for this issue](#), or go to the [journal homepage](#) for more

Download details:

IP Address: 147.102.124.92

This content was downloaded on 16/02/2016 at 10:25

Please note that [terms and conditions apply](#).

Efficient modelling of droplet dynamics on complex surfaces

George Karapetsas, Nikolaos T Chamakos
and Athanasios G Papathanasiou

School of Chemical Engineering, National Technical University of Athens, Zografou Campus 15780,
Greece

E-mail: pathan@chemeng.ntua.gr

Received 1 November 2015, revised 29 December 2015

Accepted for publication 11 January 2016


Published 1 February 2016



Abstract

This work investigates the dynamics of droplet interaction with smooth or structured solid surfaces using a novel sharp-interface scheme which allows the efficient modelling of multiple dynamic contact lines. The liquid–gas and liquid–solid interfaces are treated in a unified context and the dynamic contact angle emerges simply due to the combined action of the disjoining and capillary pressure, and viscous stresses without the need of an explicit boundary condition or any requirement for the predefinition of the number and position of the contact lines. The latter, as it is shown, renders the model able to handle interfacial flows with topological changes, e.g. in the case of an impinging droplet on a structured surface. Then it is possible to predict, depending on the impact velocity, whether the droplet will fully or partially impregnate the structures of the solid, or will result in a ‘fakir’, i.e. suspended, state. In the case of a droplet sliding on an inclined substrate, we also demonstrate the built-in capability of our model to provide a prediction for either static or dynamic contact angle hysteresis. We focus our study on hydrophobic surfaces and examine the effect of the geometrical characteristics of the solid surface. It is shown that the presence of air inclusions trapped in the micro-structure of a hydrophobic substrate (Cassie–Baxter state) result in the decrease of contact angle hysteresis and in the increase of the droplet migration velocity in agreement with experimental observations for super-hydrophobic surfaces. Moreover, we perform 3D simulations which are in line with the 2D ones regarding the droplet mobility and also indicate that the contact angle hysteresis may be significantly affected by the directionality of the structures with respect to the droplet motion.

Keywords: contact line, Cassie and Wenzel states, contact angle hysteresis, superhydrophobic surfaces

 Online supplementary data available from stacks.iop.org/JPhysCM/28/085101/mmedia

(Some figures may appear in colour only in the online journal)

1. Introduction

Contact line dynamics play a major role in a variety of industrial applications, including coating processes [1], inkjet printing [2], spray cooling [3] and microfluidic devices. Despite the huge amount of work published so far on the dynamics of wetting, a fully satisfactory and efficient physical description is still missing while the governing physical processes remain unclear [4–8] and there are still significant

challenges that need to be overcome such as the description of droplet motion on complex surfaces.

It is well known that the droplet motion along an inclined solid surface can be accompanied by the effect of contact angle hysteresis. In fact, a droplet may remain stationary below a critical inclination angle or slide at constant speed for larger angles while further increase of the inclination angle may lead to cusp formation at the rear of the droplet [9–12]; see Savva & Kalliadasis [13] for a very informative review on both the experimental

and theoretical efforts on this subject. The effect of contact angle hysteresis has been commonly attributed to the heterogeneity of the substrate or its specific structure. Since, however, in many cases the scale of roughness or chemical heterogeneity is much smaller than the characteristic size of the droplet, the most common approach on the literature is to account for the effect of hysteresis in a phenomenological way. This is typically done, both in diffuse and sharp interface models, by prescribing a static advancing and receding contact angle and assuming that when the dynamic contact angle acquires a value between these two values, there is no contact line motion. Outside this range, the dynamic contact angle may either be considered to remain fixed to the corresponding advancing or receding contact angle [14, 15] or a Cox–Voinov condition can be applied for relating the velocity of the contact line with the dynamic contact angle [16–19]. It should be noted that even though such schemes are useful in practical applications they do not offer a way to actually predict the contact angle hysteresis for a certain combination of liquid and substrate. For the latter, it has been argued that it is necessary to take into account the heterogeneity of the material and early efforts focused mainly on the effect of chemical heterogeneities [20, 21].

The modelling of spreading droplets on topographically structured substrates is significantly more challenging computationally and few theoretical studies exist in the literature, most of which were performed either by employing the lattice Boltzmann method [22, 23] or in the thin film approximation [13, 24–26]. One key difficulty in the case of complex structures is the possibility of air inclusions trapped at the solid-liquid interface which may result to the presence of multiple contact lines. For example, it has been shown that when a hydrophobic surface is covered with micro-structures the repellency may be considerably enhanced by the presence of gas pockets [27–30], limiting the contact between the liquid and the solid; this wetting state is known as Cassie–Baxter (or ‘fakir’ state) and differs from the Wenzel state in which the surface is completely wetted by the liquid. In such cases, the number of existing contact lines as well as their position cannot be known *a priori* but have to be computed as part of the solution; this can be a very difficult, if not impossible, task for the usual models based on the Cox–Voinov equation.

A related problem where a change in the topology also takes place is the case of impinging droplets on solid surfaces; a large number of experimental investigations have been reported on this subject in the literature (e.g. see [31–39] and references therein). In most practical applications the efficiency of a superhydrophobic surface relies ultimately on its ability to repel impinging drops (rain drops, sprays, etc). It has been shown that the relationship of the impact velocity and the geometric characteristics (roughness and micro-structure) of the solid surface may affect significantly the transition from a hydrophobic repellent state to a Wenzel state [40–45]. So far, due to the aforementioned difficulties on the modelling of droplet impact on structured surfaces most of the theoretical studies in the literature have focused on the study of flat surfaces [46–57]; a recent informative review on these efforts can be found in [58]. Notable exceptions of studies on the effect of surface structures

on the droplet dynamics are the works of [59–62] who employed either the volume-of-fluid (VOF) or the LB method.

An efficient methodology, using a sharp-interface model, to overcome the difficulty concerning the change in the topology of the physical domain and the presence of multiple contact lines, has been employed recently for both static and dynamic computations by Chamakos *et al* [63–65]. According to this approach, the liquid–gas and the liquid–solid interfaces are treated in a unified context (one equation for both interfaces) by employing the notion of the Derjaguin (disjoining) pressure [66] to model the micro-scale liquid–solid interactions. The main advantage of this method is that it avoids the implementation of a specific boundary condition at the contact line. The position of the contact line as well as the dynamic contact angle emerge simply as the result of the combined action of the disjoining and capillary pressure. Chamakos *et al* [65] employed this model to examine the case of a droplet impinging on (i) ideally smooth substrates with no friction and (ii) surfaces with micro-scale roughness and were able to show that in the latter case the effective shear stresses arise macroscopically due to the structure of the substrate. It should be noted, though, that although the proposed sharp-interface model appears to be quite robust for rough and complex structures, it cannot be used for the modelling of the simple case of a non-ideal flat solid surface (i.e. macroscopically smooth) without considering a geometric heterogeneity which generates friction; the term macroscopically smooth is used for a surface that is not ideal i.e. not molecularly smooth. This is clearly due to the fact that the effects of the tangential stress component of the ambient phase (i.e. the liquid–air or liquid–solid interface) have been completely ignored, thus the model predicts a shear-free flow near an ideally flat solid surface. Even though a macroscopically smooth surface could in principle be represented by a model flat surface with an arbitrary nanoscale roughness, the computational requirements for modelling contact line dynamics on such small scale roughness would be prohibitive.

The scope of the present work is to provide a generalization of the previous model [65] by introducing an effective slip length in order to provide an efficient model which takes into account the effect of friction in the case of macroscopically smooth surfaces and to enable comparisons and predictions for realistic rough or patterned substrates. This is particularly important when it comes to the study of 3D effects due to the increasing computational cost. One additional benefit is that the combination of the two approaches makes possible the modelling of flows over structures of multiple scales. The model will be implemented to examine two important cases: (i) impinging droplets on a horizontal surface and (ii) droplet motion on an inclined surface. Both cases of macroscopically flat and structured surfaces will be considered. As it will be shown below, our model compares favourably against the experimental observations for impacting droplets on smooth substrates both in terms of the spreading radius as well as the dynamic contact angle. In the case of structured surfaces it is examined under which conditions the droplet may fully wet the topography of the substrate (Wenzel state) or result in a partially wetted state (Cassie–Baxter state) with the presence of air inclusions. Another part of this work is devoted to the

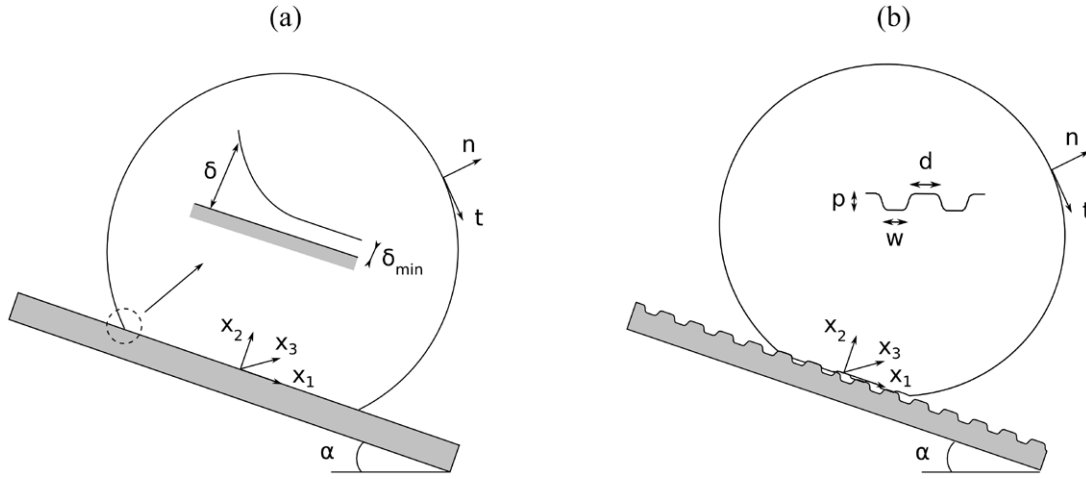


Figure 1. Schematic of a droplet sliding on a (a) flat or (b) structured solid substrate inclined at angle, α .

study of the droplet motion on a inclined surface and it is demonstrated that the model is able to provide predictions for both the static and dynamic component of hysteresis. Interestingly, it is shown that the presence of air inclusions trapped in the micro-structure of a hydrophobic substrate (Cassie–Baxter state) may result in the decrease of contact angle hysteresis and in the increase of the droplet mobility in qualitative agreement with experimental observations for super-hydrophobic surfaces. Our 3D calculations also indicate that the contact angle hysteresis is significantly affected by the directionality of the substrate topography with respect to the droplet motion.

The remainder of the paper is organized as follows. In section 2, we describe the system of governing equations and outline the numerical scheme that is used for the simulations. The results are presented and discussed in section 3. Finally, the concluding remarks are given in section 4.

2. Problem formulation

We consider the dynamics of a liquid droplet interacting with a rigid solid surface with inclination angle, α (see figure 1). The droplet is considered to be a Newtonian incompressible fluid, with nominal radius, R , density, ρ , viscosity, μ and surface tension, σ . We scale all lengths with the nominal droplet radius, R , which is defined as $R = \sqrt{A/\pi}$ for the case of 2D droplets with surface area, A , and as $R = \sqrt[3]{3V/4\pi}$ for 3D or axisymmetric droplets with volume, V . The velocities are scaled with a characteristic velocity U^* of the flow (it will be defined below depending on the problem in hand), and pressure and stresses with $\mu_1 U^*/R$. Substituting this scaling into the governing equations and boundary conditions, the dimensionless groups that emerge are the Reynolds number, $Re = \rho U^* R / \mu$, the Stokes number, $St = \rho g R^2 / \mu U^*$, and the capillary number, $Ca = \mu U^* / \sigma$.

Inserting the previously defined characteristic quantities into the momentum and mass conservation equations, we obtain:

$$Re \left(\frac{\partial \mathbf{v}}{\partial t} + \mathbf{v} \cdot \nabla \mathbf{v} \right) - \nabla \cdot \mathbf{T} + St (\cos \alpha \mathbf{e}_{x_2} - \sin \alpha \mathbf{e}_{x_1}) = 0, \quad (1)$$

$$\nabla \cdot \mathbf{v}_i = 0, \quad (2)$$

where ∇ denotes the gradient operator, \mathbf{v} is the velocity vector and \mathbf{T} is the total stress tensor

$$\mathbf{T} = -P\mathbf{I} + (\nabla \mathbf{v} + \nabla \mathbf{v}^T). \quad (3)$$

Here, P denotes the pressure and \mathbf{I} is the identity tensor.

2.1. Boundary conditions

Solution of the above set of equations is determined subject to the following boundary conditions. Following the approach of Chamakos *et al* [65] we treat the liquid–gas and liquid–solid interfaces in a unified context. Along these interfaces the flow field satisfies the local interfacial force balance between the stresses in the liquid and the ambient phase

$$\mathbf{n} \cdot \mathbf{T} = \mathbf{n} \cdot \mathbf{T}_{\text{ext}} + \frac{2\mathcal{H}}{Ca} \mathbf{n}, \quad (4)$$

where \mathbf{n} denotes the outward unit normal, \mathbf{T}_{ext} the total stress tensor of the ambient phase and $2\mathcal{H}$ is the mean curvature of the interface

$$2\mathcal{H} = -\nabla_s \cdot \mathbf{n}, \quad (5)$$

while ∇_s is the surface gradient operator, defined as

$$\nabla_s = (\mathbf{I} - \mathbf{nn}) \cdot \nabla. \quad (6)$$

Equation (4) can be rewritten as follows

$$\mathbf{n} \cdot \mathbf{T} = (\mathbf{n} \cdot \mathbf{T}_{\text{ext}} \cdot \mathbf{n}) \mathbf{n} + (\mathbf{n} \cdot \mathbf{T}_{\text{ext}} \cdot \mathbf{t}) \mathbf{t} + \frac{2\mathcal{H}}{Ca} \mathbf{n}, \quad (7)$$

where $\mathbf{n} \cdot \mathbf{T}_{\text{ext}} \cdot \mathbf{n}$ and $\mathbf{n} \cdot \mathbf{T}_{\text{ext}} \cdot \mathbf{t}$ denote the normal and tangential stress component of the ambient phase, respectively. Assuming that the viscosity of the air is negligible, the effect of the flow in the gas phase can be neglected. Moreover, following the approach of Chamakos *et al* [65] the normal micro-scale liquid–solid interactions are introduced through a disjoining pressure term, Π , which accounts for the presence of antagonistic short- and long-range intermolecular forces

$$\mathbf{n} \cdot \mathbf{T}_{\text{ext}} \cdot \mathbf{n} = -P_g + \Pi, \quad (8)$$

where

$$\Pi = \frac{w_{ls}}{\text{Ca}} \left[\left(\frac{A}{\delta + \epsilon} \right)^{C_1} - \left(\frac{A}{\delta + \epsilon} \right)^{C_2} \right]. \quad (9)$$

A similar approach has been used widely in the literature for the modelling of contact lines in thin film flows [67–69], however as it was shown by Chamakos *et al* [64, 65, 70] its applicability can be far more generic. The idea is to use a Lennard–Jones type potential (equation (9)) (not to be confused with the conventional 12-6 L–J potential) as a simple way to approximate strong repulsion at short distances between the liquid and the solid phases, and attraction at intermediate distances. The action of the potential is taken into account only along the interface and its range is small compared to both droplet radius and the scale of solid structures.

The wetting parameter, w_{ls} , (in equation (9)) is directly related with the substrate wettability through the following relation

$$\cos \theta_Y = \frac{w_{ls}(C_1 - C_2)A}{(C_1 - 1)(C_2 - 1)} - 1, \quad (10)$$

where θ_Y denotes the Young equilibrium contact angle and the exponents C_1 and C_2 control the range of the micro-scale liquid/solid interactions; large values of C_1 and C_2 reduce the range within which micro-scale interactions are active. In equation (9), δ denotes the distance of separation between the solid and the liquid surface and in the case of a perfectly flat solid surface, δ is simply defined as the vertical distance of the liquid surface from the solid boundary (see figure 1(a)). The minimum distance of separation, δ_{\min} , between the liquid and the solid phase (the distance at which the interaction forces between liquid and solid are minimized) is controlled by the constants A and ϵ , i.e. $\delta_{\min} = A - \epsilon$. For the simulations that will be presented below we consider the disjoining pressure constants value in accordance with previous studies [64, 65], namely: $C_1 = 12$, $C_2 = 10$, $A = 0.009$, $\epsilon = 0.008$, unless noted otherwise.

For the purposes of their study, Chamakos *et al* [65] ignored the effect of the tangential stress component of the ambient phase, $\mathbf{n} \cdot \mathbf{T}_{\text{ext}} \cdot \mathbf{t}$, considering a shear-free condition. Here, a generalised boundary condition will be considered that incorporates the possibility of partial fluid slip along the solid boundary, by introducing the Navier slip model. According to this model, it is assumed that the velocity along the solid surface is proportional to the shear stress at the surface

$$\mathbf{n} \cdot \mathbf{T}_{\text{ext}} \cdot \mathbf{t} = \beta_{\text{eff}}(\mathbf{t} \cdot \mathbf{v}), \quad (11)$$

where β_{eff} denotes the effective slip coefficient (i.e. the scaled inverse slip length). Since our formulation treats the gas and solid phase in a unified context, a continuous function is needed and the following expression is employed

$$\beta_{\text{eff}} = \beta_{\text{sl}} \left(1 - \tanh \left[5 \left(\frac{\delta}{\delta_{\min}} - 1 \right) \right] \right). \quad (12)$$

β_{sl} is a parameter which accounts for the adhesion properties of the liquid droplet on the solid surface. According to equation (12) β_{eff} is equal to β_{sl} along the liquid–solid interface

(for $\delta \approx \delta_{\min}$) and zero everywhere else implying a shear-free boundary condition along the liquid–gas interface; this variation takes place at a smaller length scale than the action of the disjoining pressure. If β_{sl} acquires very large values ($\beta_{\text{sl}} \gg 1$) we recover the usual no-slip boundary condition along the liquid–solid interface (from equation (11) if $\beta_{\text{eff}} \gg 1$ then $\mathbf{t} \cdot \mathbf{v} \approx 0$) whereas for moderate values of this parameter partial slip is allowed. In contrast to [65], the present model allows to account for the effect of friction that the liquid may experience on macroscopically flat solid surfaces without having to take into account their micro-structure. The main benefit, however, is that by combining these two approaches, i.e. taking into account the large scale structure of the substrate topography and employing equation (11) to account for the smaller scale structures, it becomes possible to model efficiently structures of multiple scales. Such an approach has been used for the 2D calculations presented in section 3.2.2 below.

Along the moving interface we impose the kinematic boundary condition,

$$\mathbf{v}_{\text{mesh}} = \mathbf{v} \cdot \mathbf{n}, \quad (13)$$

where \mathbf{v}_{mesh} is the velocity of the mesh at the interface. Finally to complete our model, it is necessary to set a datum pressure and as such, the pressure in the gas phase is imposed to be equal to zero $P_g = 0$, without loss of generality.

2.2. Model of the substrate topography

2.2.1. Explicit model for geometrical pattern. As it was noted above, for the purposes of this study both cases of a macroscopically flat and a structured solid surface will be examined. The model for the former case is quite straightforward and has been described above. For the case of a patterned solid surface we will follow two alternative routes.

The first approach is to consider explicitly the topography of the solid surface (see figure 1(b)) and this is taken into account by describing the roughness of the solid using the following expression

$$h(x_1) = \frac{p}{2} \left[\tanh \left(\frac{x_1 - (d + w/2)}{s} \right) - \tanh \left(\frac{x_1 - w/2}{s} \right) \right], \quad (14)$$

where w and d denote the width of troughs and crests, respectively, p denotes the height of the protrusions and s is a regularization parameter. Above, it has been mentioned that for the case of a flat substrate the distance, δ , in equation (9) can be taken to be equal to the vertical distance from the solid surface. In the case of patterned surfaces the definition of distance, δ is not straightforward and requires special consideration. Here we follow the approach of Chamakos *et al* [63–65] taking δ to be equal to the minimum distance from the solid which is obtained by solving the eikonal equation [71]. This approach will mainly be used for the 2D simulations presented below.

2.2.2. Emulate pattern with varying material properties in space. Despite the efficiency of the method described above, the computational cost becomes significantly high when it comes to the study of droplets on surfaces with 3D patterns.

To overcome this difficulty, we also propose a slightly different approach which will be used for our 3D simulations (see section 3.2.3 below). Here, the focus will be on cases where the droplet is in ‘fakir’ state, where the presence of air pockets within the roughness acts as effective ‘shear free’ regions. To account for this effect, we adopt an approach which is similar to some extent to the approach presented by [20, 21] in their effort to model the effect of chemical heterogeneities on the spreading of thin droplets. In this work the substrate was considered to be flat and the effect of chemical heterogeneity was introduced by taking the equilibrium contact angle to be a custom function of the substrate coordinates. More specifically, we assume that the regions of the liquid interface above the gas pockets are described by negligible shear stress and that the equilibrium apparent contact angle between the liquid and the substrate becomes equal to 180° . In the regions where the liquid is in contact with the solid we apply the Young contact angle and a finite value for the slip coefficient, β_{sl} . To achieve this we introduce a function of the substrate coordinates for the slip coefficient and wettability of the substrate and redefine the parameters w'_{ls} and β'_{sl} as follows

$$w'_{ls} = w_{ls}f(x_1, x_3) \quad (15)$$

$$\beta'_{sl} = \beta_{sl}f(x_1, x_3) \quad (16)$$

where $f(x_1, x_3)$ is a function that describes the pattern of the substrate. To this end, the following equation is solved

$$\nabla^2 f(x_1, x_3) = 0, \quad (17)$$

while setting appropriate boundary conditions to generate the desired pattern. To indicate at a certain position the presence of the solid surface we impose f to be equal to 1 (grey areas in figures 13(a)–(c) below), while f is imposed to 0 to indicate the presence of gas pockets (white areas in figures 13(a)–(c)).

2.3. Numerical implementation

The above set of equations is combined with an elliptic grid generation scheme capable of following the deformations of the physical domain [65, 72]. In order to resolve adequately the flow, the mesh is refined around the moving liquid–air or liquid–solid interface; a typical grid is presented in figure 2. The set of algebraic equations is integrated in time with the implicit Euler method. The model has been implemented in COMSOL Multiphysics® commercial software and has been cross-checked against our in-house FEM solver [73].

3. Results

3.1. Impact of an axisymmetric droplet onto a rigid solid surface

We begin our study by examining the flow dynamics of an impinging axisymmetric liquid droplet on a horizontal surface ($\alpha = 0^\circ$) and by comparing against the experimental data presented by Šikalo *et al* [31]. Chamakos *et al* [65] have shown that it is possible to model these experimental observations simply by taking into account the ever present roughness of

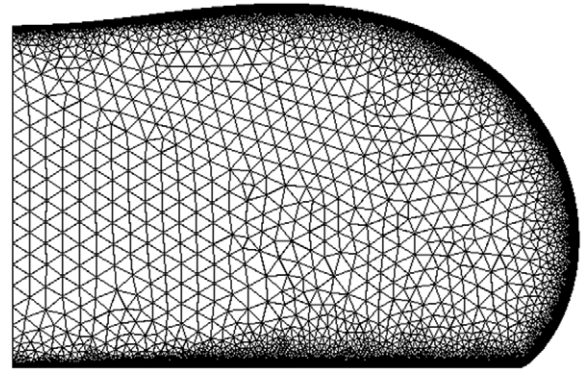


Figure 2. Typical grid of an axisymmetric droplet impacting on a flat solid surface.

Table 1. Liquid droplet properties, size, impact velocity and corresponding dimensionless numbers.

Glycerin/water mixture	R ($\times 10^{-3}$ m)	V_{imp} ($m\ s^{-1}$)	Re	Ca	St
$\rho = 1220\ kg\ m^{-3}$	1.225	1.037	13.36	1.91	0.15
$\mu = 0.116\ Pa\ s$	1.225	1.400	18.04	2.58	0.11
$\sigma_{la} = 0.063\ N\ m^{-1}$	1.225	4.111	52.97	7.57	0.04

a real solid substrate. This approach, however, may become quite computationally demanding when the disparity between the scale of roughness and droplet size becomes large. In this case it makes sense to consider the case of a macroscopically flat surface and introduce the effect of friction through equation (11) as explained above. Clearly, by combining these two approaches it may also become possible to model structures of multiple scales.

Here, we consider the case of a glycerin/water mixture droplet (85% of glycerin) which impacts vertically a wax surface. The properties of the droplet as well as the corresponding dimensionless numbers obtained using these parameters are given in table 1. For the scaling of the governing equations and the evaluation of the dimensionless groups we use as characteristic velocity, U^* , the impact velocity of the droplet, U_{imp} . For all the simulations presented below, we consider that the drop initially is spherical at a small distance above the horizontal solid surface; the initial distance between the lowest part of the drop and the solid is considered to be 0.005. Note that the effect of air layer below the droplet, which can be potentially important [74, 75], has been ignored in the present study. It should be mentioned, though, that this is by no means a restriction of the present formulation since it is quite straightforward to introduce the presence of air into our model.

3.1.1. Validation with experimental data on a macroscopically smooth substrate. To set the stage for the discussion that follows, it is useful to examine first the case that has been examined by Chamakos *et al* [65], i.e. for $U_{imp} = 1.037\ m\ s^{-1}$. Figure 3 presents the temporal evolution of the contact radius and dynamic contact angles for different values of the slip parameter, β_{sl} . The solid line corresponds to the results obtained by [65] for a flat substrate (for $\beta_{sl} = 0$) whereas the

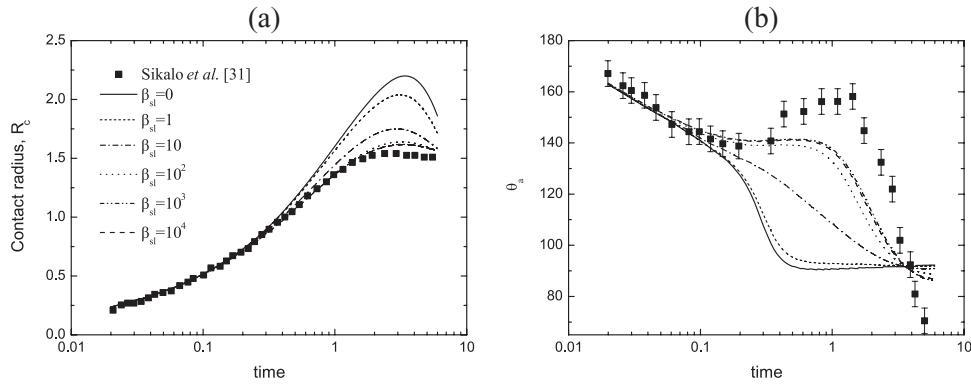


Figure 3. Evolution of the (a) contact radius and (b) dynamic contact angle of an impinging glycerin/water (85%) mixture droplet on wax surface: experimental data from Sikalo *et al* [31] against simulations for different values of the slip coefficient, β_{sl} , and $Re = 13.36$, $Ca = 1.91$, $St = 0.15$ and $\theta_Y = 93.5$. The dynamic contact angle is evaluated at height 0.01 from the substrate.

square symbols correspond to the experimental data presented by [31]. It is shown that for finite values of the slip coefficient, β_{sl} , the droplet decelerates faster (see figure 3(a)) and this is due to the friction that the fluid experiences along the contact area with the solid surface. Increasing the value of β_{sl} the boundary condition that is applied in the region of the solid wall turns gradually from a shear-free condition to an essentially no-slip boundary condition for large values of β_{sl} (see equation (11)). As it is shown in figure 3(b), apart from the contact line radius, the slip coefficient affects significantly the dynamic contact angle. In the case of perfect slip, the dynamic contact angle very soon attains the value of the equilibrium contact angle whereas increasing the value of β_{sl} the model follows much closer the experimental data. For large values of β_{sl} ($\beta_{sl} > 10^3$) the effect of friction on the flow dynamics is negligible since $\beta_{sl} \approx 10^3$ appears to be sufficient in order to recover the no-slip boundary condition along the solid surface and hence to describe adequately the flow near a rough surface; this in agreement with the findings of Chamakos *et al* [65] who noted that beyond a certain roughness factor threshold the flow dynamics remain practically unaffected. In dimensional terms, given that the size of the droplet radius is approximately equal to 1 mm, $\beta_{sl} \approx 10^3$ – 10^4 corresponds to a dimensional slip length of 0.1–1 μm which is roughly of the same order with the roughness of the wax surface used by Sikalo *et al* [31].

At this point we should note that although the agreement of our results (assuming $\beta_{sl} = 10^3$) with the experimental data is very good for the major part of the simulation, a discrepancy arises at late times (see figure 3(b)). This could be attributed to our assumption of a macroscopically flat substrate since as it is shown in [65] for a microscopically rough substrate the simulation follows more closely the experimental data. At late times the droplet reaches its maximum radius and the flow decelerates significantly as it enters the phase of recoil. At that point the geometrical characteristics of the solid surface become increasingly important since the flow becomes very slow and the droplet has the time to adjust to the roughness of the substrate. The latter effect may actually lead to the pinning of the contact line which explains the appearance of a local maximum of the dynamic contact angle at late times before the droplet starts to recoil. Clearly this effect cannot be

taken into account when considering a macroscopically flat substrate unless this is done e.g. by introducing the effect of chemical heterogeneities along the solid surface [20, 65].

To examine the predictive capability of our model we fix for the remaining part of our study the value of the slip coefficient, β_{sl} , which we consider to be a parameter that characterizes the substrate, to $\beta_{sl} = 10^3$. In figure 4 we present the dynamics of the same impinging droplet for three different impact velocities and compare against the experimental data of [31]. As it is shown, without any other fitting, the model is able to describe very well the dynamics of spreading even at high values of the Re and Ca numbers, except for the very late stages of the flow for the reasons mentioned above. In the case of highest impact velocity we also note a discrepancy that arises in the prediction of the dynamic advancing contact angle at early times which can potentially be attributed to the effect of the surrounding air which has been ignored in the present study.

3.1.2. Impact on a patterned substrate. Now that we have demonstrated that the proposed scheme can describe adequately the experimental observations for a macroscopically flat substrate, we continue our study by examining the case of a droplet impinging on a structured substrate. Here, the large-scale pattern of the solid surface is described by equation (14), while the dissipative effect of the micro-scale roughness is taken into account through the use of a finite slip coefficient, β_{sl} . For the calculations to be presented in this section, the width of troughs and crests are considered to be $w = 0.1$ and $d = 0.1$, respectively, while the value of the regularization parameter is $s = 0.02$; (for a millimeter sized droplet this corresponds to widths of $\sim 100 \mu\text{m}$).

In figure 5 we present a simulation of a droplet impinging on a surface with stripes of height $p = 0.07$ for $Re = 1$ and $Ca = 0.7$; the corresponding value of the Weber number, which represents a measure of the relative importance of the fluid's inertia compared to its surface tension, is equal to $We = ReCa = 0.7$. As the droplet impacts the surface, it decelerates near the solid surface and soon after the droplet comes into contact with the solid, it impregnates the two grooves near the center; figure 5(d) depicts a contour plot of the axial velocity field and the streamlines at $t = 0.3$ in a

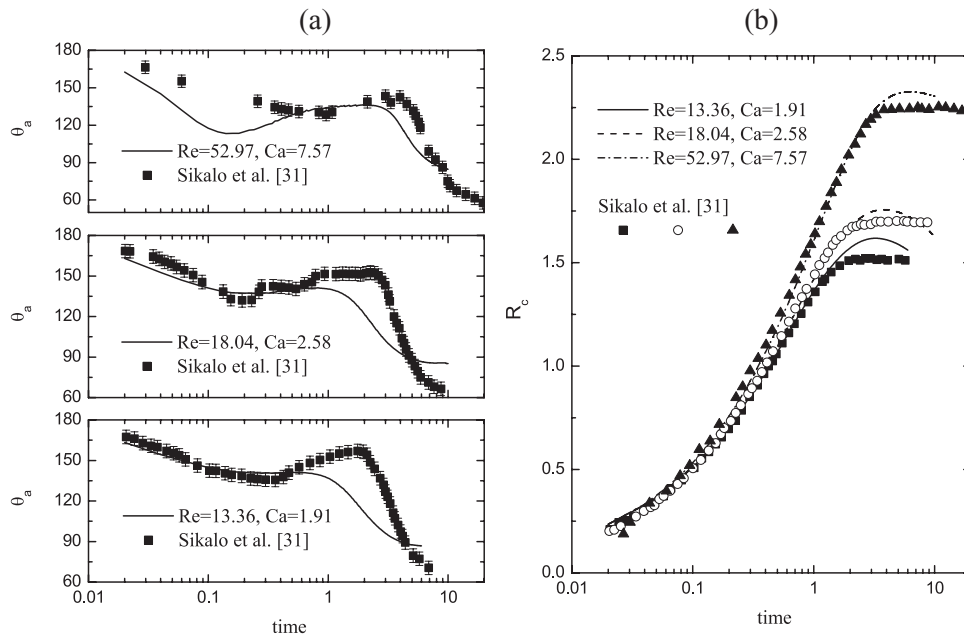


Figure 4. Evolution of the (a) dynamic contact angle and (b) contact radius of glycerin/water (85%) mixture droplet impinging on a horizontal wax surface with various impact velocities for $\theta_Y = 93.5$ and $\beta_{slip} = 10^3$. Comparison with experimental measurements by Sikalo *et al* [31].

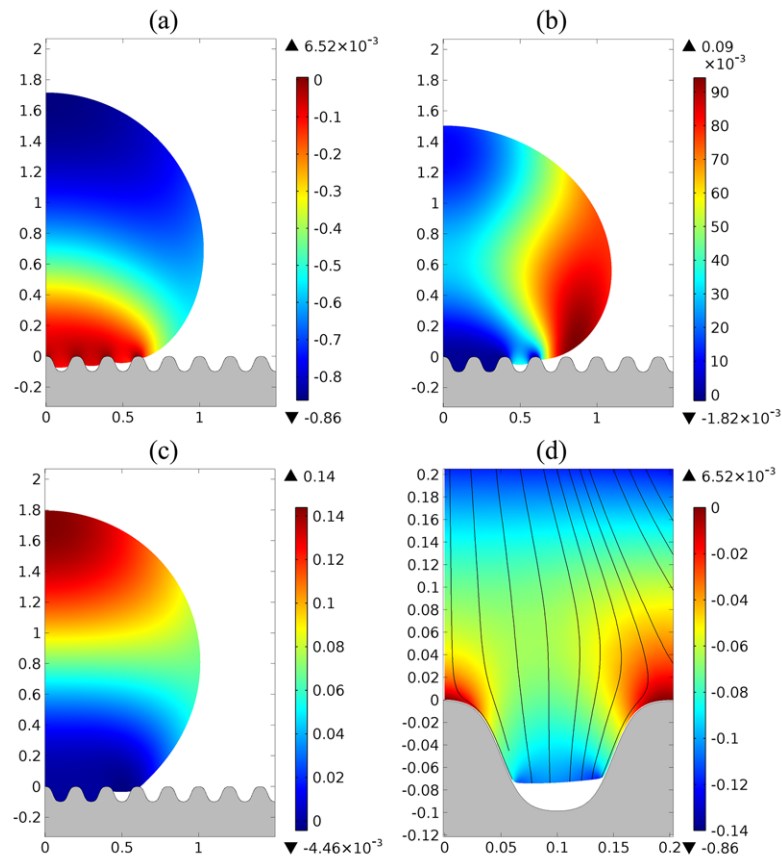


Figure 5. Contour plots of the axial velocity at (a) $t = 0.3$, (b) $t = 0.8$ and (c) $t = 2$ for a droplet impinging on a structured substrate with $\theta_Y = 120^\circ$. Panel (d) depicts a zoom of the axial velocity fields and the streamlines inside the first groove near the center at $t = 0.3$. The remaining parameters are $Re = 1$, $Ca = 0.7$, $\beta_{slip} = 10^3$, $w = 0.1$, $d = 0.1$, $p = 0.07$.

zoomed area inside the first groove near the axis of symmetry, as the impalement takes place. Apparently, the capillary forces in the groove cannot resist the dynamic pressure acting at the

liquid–gas interface and the latter collapses. This is not the case, however, in the outer groove which is only partially wetted by the liquid even at late times (see figure 5(c)).

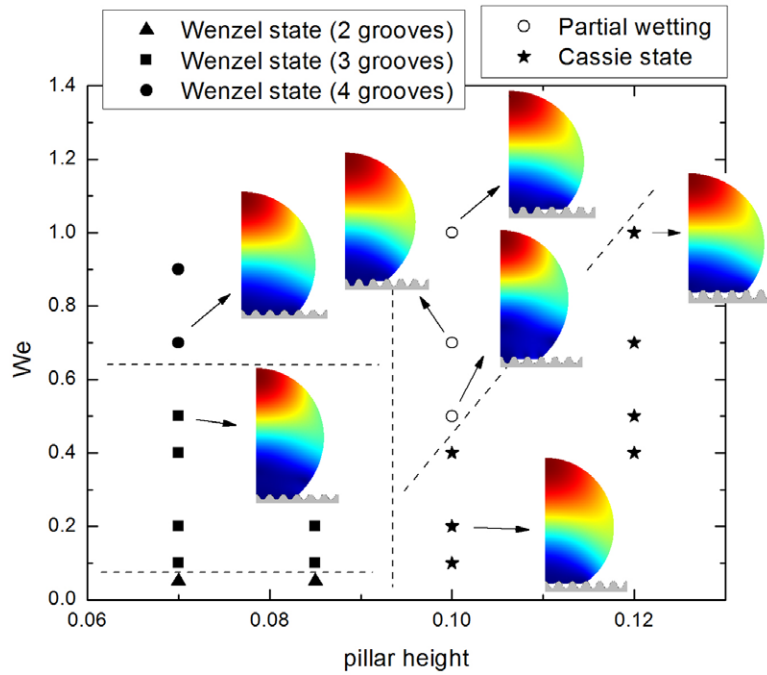


Figure 6. Flow map with different resulting states of an impinging droplet on a structured surface for various values of the We number and pillar heights, p . The remaining parameters are $Re = 1$, $\theta_Y = 120^\circ$, $\beta_{\text{slip}} = 10^3$, $w = 0.1$, $d = 0.1$.

In order to investigate further the predictions of our model, we produced a flow map presented in figure 6 where we examine the final droplet state for various values of the We number and pillar heights, p . As expected, for small pillar heights the droplet fully wets the topography of the solid surface even in cases where the kinetic energy of the droplet is relatively small (low value of We). The number of pillars that will be wetted and consequently the resulting apparent contact angle, however, depends on the actual value of the We number. On the other hand, for pillars of large height the droplet ends up in a ‘fakir’ state and the range of We number where this ‘fakir’ state is possible increases with increasing height of the pillars. Nevertheless, when the kinetic energy of the droplet is large (high values of We) the ‘fakir’ state can no longer be sustained and partial wetting is observed. These results are in line with the experimental observations in the case of bouncing droplets [40, 41, 76] where typically pinning of the droplet takes place provided the impact velocity is large enough, due to the collapse of the liquid–gas interface in the structures of the solid wall, while it is hindered by the presence of tall structures due to the persistence of the ‘fakir’ state of the droplet. The three distinct regions, shown in figure 6, correspond to the three different wetting states predicted by Deng *et al* [77], i.e. the total non-wetting state (‘fakir droplet’), the total wetting state and the partial wetting state, where the liquid penetrates into the internal grooves of the striped surface while it partially penetrates into the external grooves leaving their ground dry. Note that, the presence of such intermediate states has also been confirmed recently both by static and dynamic computations [62, 70].

The ability of the proposed scheme, given its simplicity and robustness, to model efficiently cases with multiple contact lines and the ability to handle a change in the topology

could prove useful in many engineering applications where e.g. it is desired to design surfaces so that drops do not adhere to them but instead bounce off, due to their ability to stay dry, self-clean or resist icing.

3.2. Droplet spreading on an inclined surface

We continue by investigating the predictions of our model for a droplet sliding on an inclined flat or structured substrate. Note that for this part of our study we consider a different scaling for the velocity field. In contrast to the above section, here a characteristic velocity does not exist and as such we use instead $U^* = \sqrt{gR}$. Under this formulation, the Re and St numbers, as defined in section 2, both reduce to the Archimedes number, $Ar = \rho\sqrt{gR^3}/\mu$. Regarding the initial condition, for all the simulations presented below we consider that the drop initially rests at equilibrium on a horizontal solid surface before the solid becomes inclined at angle, a .

3.2.1. Cylindrical (2D) droplet on a macroscopically flat substrate. First we examine the simplest case of cylindrical (2D) droplet on a macroscopically flat substrate. For the simulations presented in figure 7 we consider the same glycerin/water mixture droplet (85% of glycerin) as above (properties and size of the droplet are given in table 1) resting on a surface with $\theta_Y = 93.5^\circ$. At $t = 0$ the surface is inclined at 45° and the droplet starts to slide due to the effect of gravity. The contour plot of the radial velocity at a late time instant ($t = 30$), i.e. when the drop has reached a steady motion, is presented in figure 7(a), while the evolution of the dynamic advancing and receding contact angles are plotted in figure 7(b). As it is shown, the interplay of the liquid motion with the solid surface, and in particular the friction that the liquid experiences

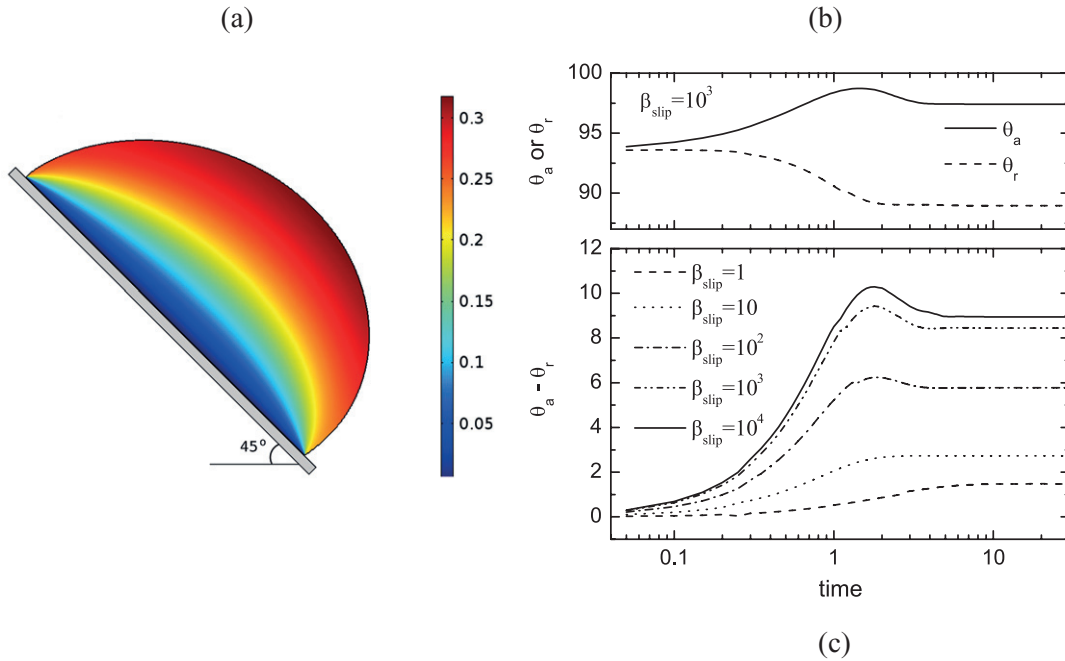


Figure 7. Glycerin/water (85%) mixture droplet sliding on an inclined (45°) wax surface; $Ar = 1.413$, $Ca = 0.202$ and $\theta_Y = 93.5$. (a) Long time shape and contour plot of the radial velocity, u_r , at $t = 30$. Evolution of (b) the dynamic advancing and receding contact angles for $\beta_{sl} = 10^3$ and (c) the contact angle hysteresis for various values of β_{sl} .

along the solid gives rise to dynamic hysteresis which is naturally predicted by our model. For this particular case, the difference between the dynamic advancing and receding contact angles at late times amounts to approximately 9° . As expected, we find that the prediction for contact angle hysteresis depends significantly on the value of β_{sl} which controls the amount of friction that the fluid experiences (see figure 7(c)). For $\beta_{sl} = 0$ (full slip) there is no hysteresis whereas for large values of this parameter the dynamic hysteresis appears to converge to a limiting value.

It is important to note that, although the proposed model has a built-in capability to predict the effect of dynamic hysteresis, in the case of a macroscopically flat surface it does not provide a prediction for the static contact angle hysteresis which is often observed in experiments. This is due to the fact that, according to equation (11) and for a homogeneous substrate, if there is no motion there is no resisting force to gravity which implies that the droplet will slide for arbitrarily low inclination angles, albeit with a very small velocity. As it will be shown below, the effect of static hysteresis can be predicted by our model, e.g. by taking into account the effects of a structured substrate.

3.2.2. Effect of substrate topography: cylindrical (2D) droplet.

Here, we examine the case of structured substrates and the effect of topography on the induced contact angle hysteresis and flow dynamics. In figure 8 we present the case of a droplet sliding on a surface with trapezoid structures. We select a case with rather shallow structures in order to create a surface that macroscopically looks smooth; the width of troughs and crests are $w = 0.02$ and $d = 0.02$, respectively, while the height of the protrusions is $p = 0.005$, see equation (14); the value of the regularization parameter is $s = 0.004$. Figure 8(a)

depicts the evolution of the dynamic advancing and receding contact angles for two different inclination angles. When the substrate is tilted at 10° , the droplet rearranges from its equilibrium shape and the apparent advancing and receding contact angles diverge from their initial equilibrium values which for this case is approximately equal to 124.5° . The front part of the droplet initially spreads along the solid surface while the rear part of the drop remains pinned. The high frequency oscillations of the advancing contact angle (see figure 8(a)) are due to the reconfiguration of the liquid–air interface as the droplet spreads along the asperities of the substrate. After this initial phase of elongation the droplet soon reaches a new equilibrium state and remains stationary thereafter. Clearly, in the case of a structured substrate the model predicts the effect of static hysteresis, unlike the case of a macroscopically flat substrate where no static hysteresis is predicted. From our calculations we evaluate the static contact angle hysteresis to be approximately equal to 33° .

Increasing the inclination angle to $a = 15^\circ$ the droplet starts to slide along the solid surface and acquires a constant average velocity; the contour plot of the radial velocity at $t = 30$ is depicted in figure 8(b). Due to the finite size of the asperities of the solid substrate the droplet does not reach an actual steady state since the liquid–air interface exhibits an oscillatory behaviour as the droplet moves along them; this is clearly reflected on the evolution of the advancing and receding contact angles shown in figure 8(a). The average contact angle hysteresis for this case is found to be approximately equal to 41° which results from the contributions of both static and dynamic hysteresis. It should also be noted that for the specific simulation the slip coefficient was taken to be equal to $\beta_{sl} = 0$ while calculations for finite values of β_{sl} (e.g. $\beta_{sl} = 10^3$) led to negligible differences (not shown here

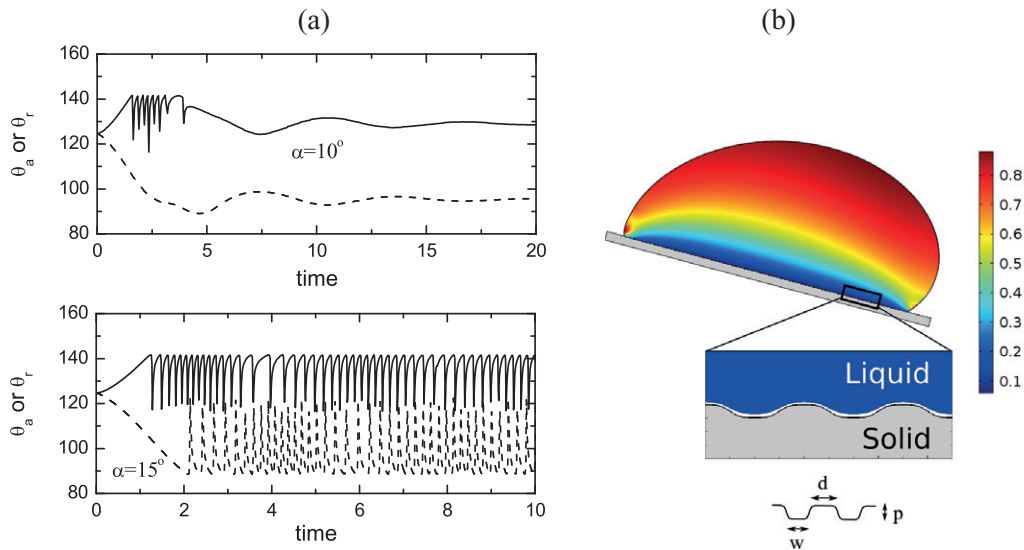


Figure 8. (a) Evolution of the dynamic contact angles for two different inclination angles (top: $\alpha = 10^\circ$, bottom: $\alpha = 15^\circ$) and (b) contour plot of the radial velocity, u_r , at $t = 10$ of a droplet sliding on an inclined (15°) surface; $Ar = 10$, $Ca = 0.1$, $\theta_Y = 117^\circ$, $\beta_{sl} = 0$, $w = 0.02$, $d = 0.02$ and $p = 0.005$.

for conciseness). This is due to the fact that the effective shear stresses arise macroscopically simply because of the structure of the substrate and essentially give rise to a no-slip boundary condition at the wall even for $\beta_{sl} = 0$.

Lately, there has been increased interest in super-hydrophobic surfaces for their ability to repel liquid water and increase drop mobility. It has been shown that when a hydrophobic surface is covered with micro-structures the repellency may be considerably enhanced by the presence of gas pockets trapped at the solid-liquid interface [29, 30], limiting the contact between the liquid and the solid. To examine whether this behaviour can be predicted by our model we consider two surfaces with smooth protrusions, the geometrical characteristics of which are shown in figure 9. In both cases we consider protrusions of the same maximum height ($p = 0.04$) and vary the shape and distance between the protrusions in order to favour either the Wenzel wetting state (figure 9(a)) or the Cassie–Baxter wetting state (figure 9(b)); we also assume that the material is very hydrophobic ($\theta_Y = 130^\circ$). In the former case the width between the protrusions is 0.2 (the distance between two successive peaks) whilst in the latter the stripes are closer to each other with a maximum width of 0.12. The roughness factor, defined as the ratio of the actual over the apparent surface area, is evaluated to be approximately equal to $r_f = 1.12$ and $r_f = 1.49$, respectively.

Starting from the equilibrium state (at $t = 0$ the inclination angle is $a = 0^\circ$) the droplet is inclined at $a = 60^\circ$. Naively, one would expect that the droplet mobility would decrease in the case of high r_f value since we would expect that viscous dissipation would be more enhanced on a rougher surface. However, as it is shown in figure 9 the opposite is actually found to be true since it is shown that at $t = 6$ the droplet actually covers larger distance in figure 9(b) than in figure 9(a). The difference of the center of mass velocity between these two cases is depicted in figure 10(a). To rationalize this behaviour we must look closer to the liquid–solid interface. As it is

shown in figure 9(a) the liquid has impaled the solid roughness whereas in figure 9(b) the droplet sits on top of the protrusions minimizing the contact between the liquid and the solid surface and therefore leading to increased mobility of the droplet, in agreement with experimental observations [29, 30, 78, 79]. It should be noted that the presence of gas pockets (shown in figure 9) has not been predefined in any way but is actually predicted by the model given the geometry of the specific substrate topography.

In figure 10(b) we examine the evolution of the dynamic advancing and receding contact angles. At the early stages of spreading, the period of oscillations for the advancing contact angle is smaller than for the receding contact angle. This is due to the fact that at this stage the droplet elongates and wets more pillars at the front than at the rear. After some time, the droplet ceases to elongate and reaches a quasi-steady state motion while the oscillations of both contact angles become in-phase. For the ‘fakir’ droplet we find that the average dynamic hysteresis is approximately equal to 48° whereas for the Wenzel state is 57° , suggesting that air inclusions indeed result in the decrease of the contact angle hysteresis. Experimentally it has been observed that the contact angle hysteresis in the ‘fakir’ regime is generally very low (about 5° – 10°) [80]. In our case, however, the scale of the substrate structures, although it is relatively small it is still comparable to the size of the droplet and it has been argued that for meaningful measurements of apparent contact angles, the drops should be much bigger (probably by three orders of magnitude) than the scale of roughness or chemical heterogeneity [81]; this condition is clearly not met in our simulations. Moreover, our 3D simulations, which are presented below, seem to indicate that the type and directionality of the structures with respect to motion of the droplet also play an important role and should be taken into account. Nevertheless, the prediction of the decrease of the dynamic hysteresis in the case of a ‘fakir’ droplet is encouraging and evidently in qualitative agreement with

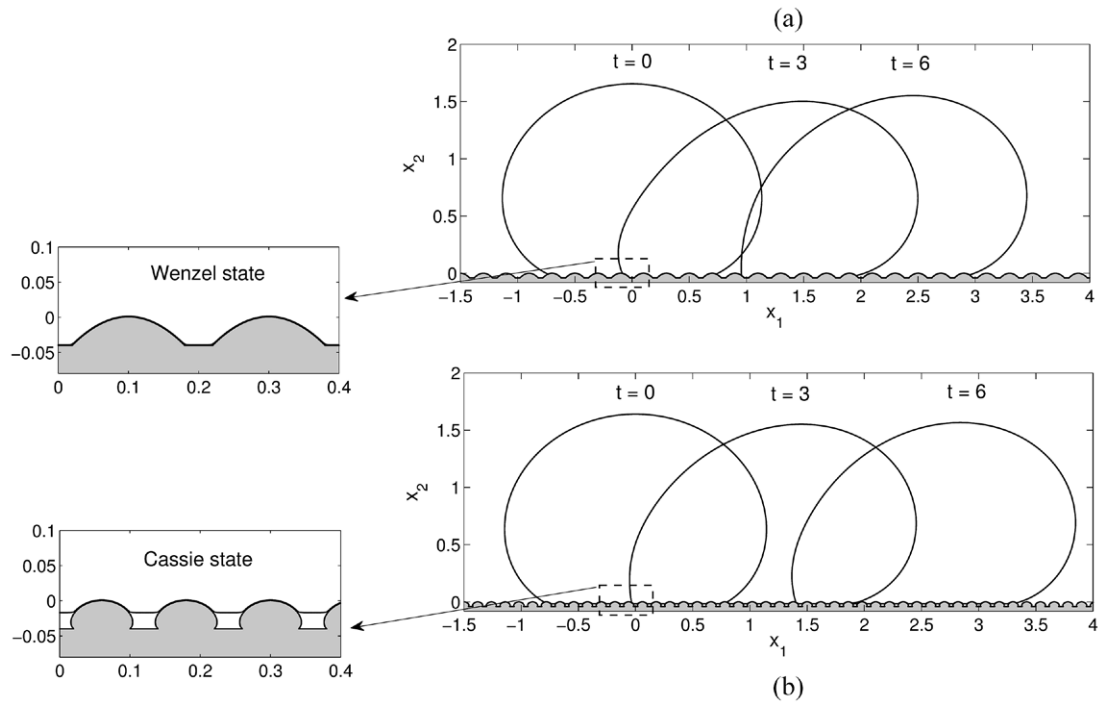


Figure 9. Droplet profiles at $t = 0, 3$ and 6 for a droplet sliding on a inclined structured substrate (60°) which promotes (a) the Wenzel wetting state and (b) the Cassie–Baxter wetting state; $Ar = 2$, $Ca = 0.2$, $\theta_Y = 130^\circ$ and $\beta_{sl} = 10^3$. An animation of the present simulation is given in stacks.iop.org/JPhysCM/28/085101/mmedia.

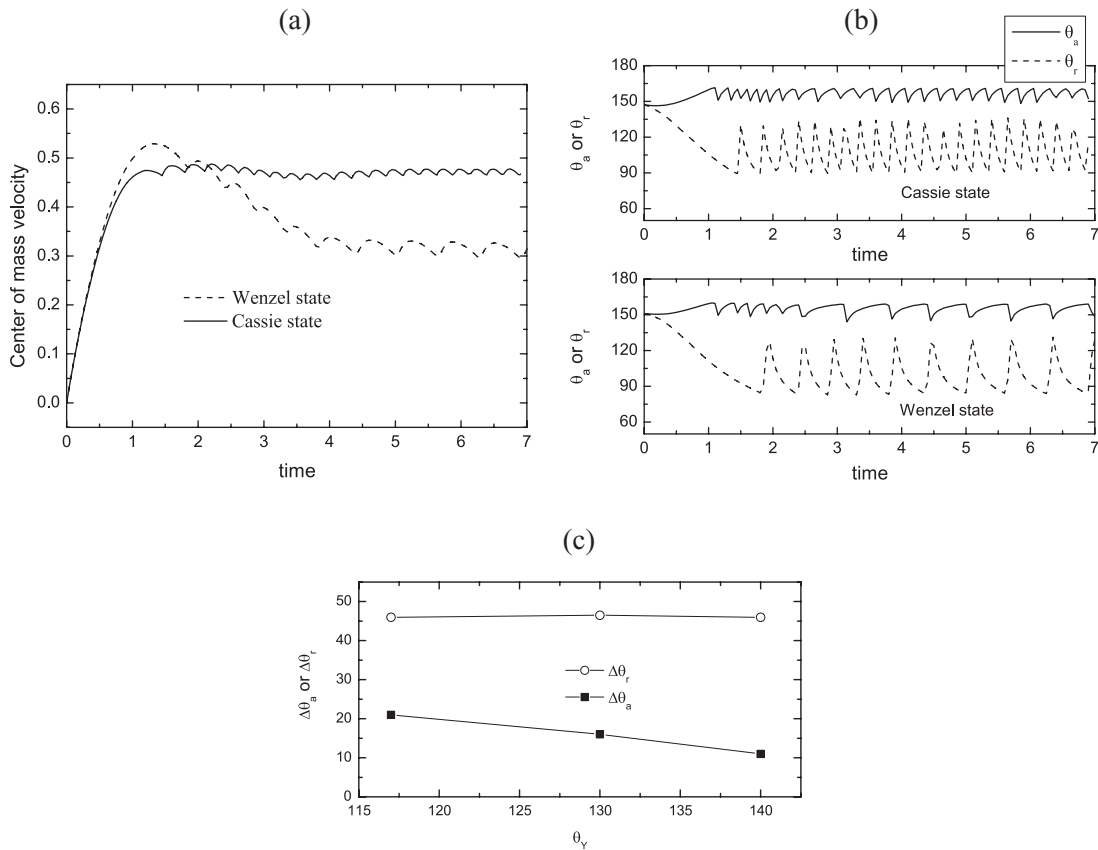


Figure 10. Evolution of the (a) center of mass velocity and (b) dynamic advancing and receding contact angles for two different geometries. (c) Dependence of the oscillation amplitude of the dynamic advancing and receding contact angles ($\Delta\theta_i = \theta_{i,max} - \theta_{i,min}$, $i = a, r$) on the material wettability, θ_Y . The remaining parameters are $Ar = 2$, $Ca = 0.2$, $\theta_Y = 130^\circ$, $\beta_{sl} = 10^3$ and $a = 60^\circ$.

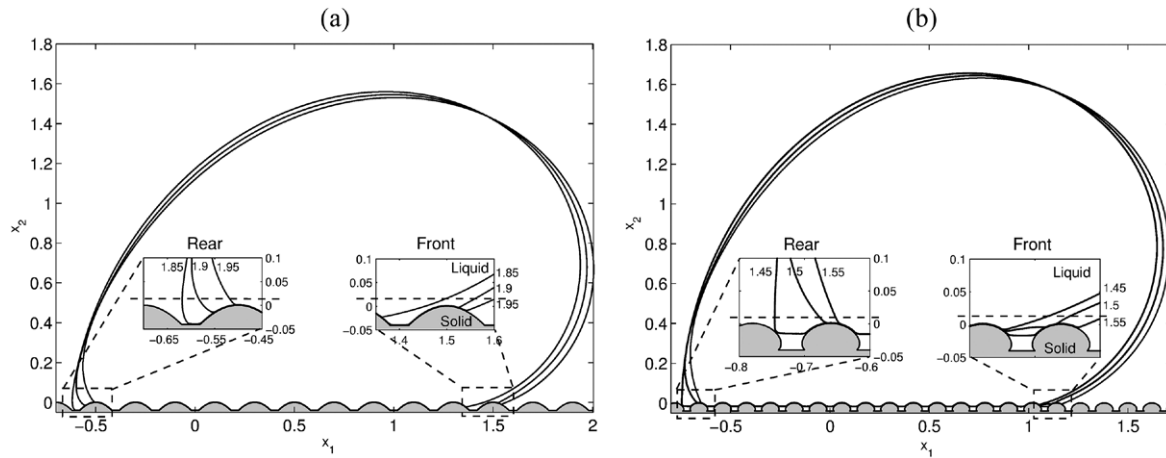


Figure 11. Profiles of a droplet sliding on an inclined structured substrate (60°) which promotes (a) the Wenzel wetting state at $t = 1.85, 1.9$ and 1.95 and (b) the Cassie–Baxter wetting state at $t = 1.45, 1.5$ and 1.55 ; $Ar = 2, Ca = 0.2, \theta_Y = 130^\circ$ and $\beta_{sl} = 10^3$. The insets depict a zoom near the front and rear contact lines and the horizontal dashed lines indicate the baseline where the contact angles are evaluated.

experiments. We should note at this point that in an attempt to model a case of super-hydrophobic surface with hierarchical topographical features, we have also performed a simulation for a case similar to figure 9(b) assuming $\theta_Y = 150^\circ$; we used a higher value for θ_Y to indicate that the contact angle will be increased due to the presence of small-scale structures. Interestingly, it is found that in this case the predicted value of the average dynamic hysteresis decreases significantly (it is found to be approximately equal to 5°) as expected and in line with experimental observations.

Another interesting observation is the fact that in both cases shown in figure 10(b), the sharp oscillations of the dynamic advancing contact angle have smaller amplitude than the ones of the receding contact angle. Clearly, one factor that plays a significant role is the shape and size of the substrate structures. As it was shown in figure 8, for structures with relatively small height the oscillation amplitude does not vary significantly between the advancing and receding contact line regions, whereas for taller structures, as in figure 10, this is clearly not the case. Our simulations also indicate that another factor that plays a role is the equilibrium contact angle of the substrate. Figure 10(c) depicts the dependence of the average oscillation amplitude of the dynamic advancing and receding contact angles ($\Delta\theta_i = \theta_{i,max} - \theta_{i,min}, i = a, r$) on the value of the equilibrium contact angle, θ_Y . Interestingly, we find that the oscillation amplitude of the advancing contact angle decreases with increasing θ_Y in contrast to the amplitude of the receding contact angle which remains practically unaffected.

To rationalize this behaviour we need to look in detail the pinning and de-pinning process as the droplet slides along the asperities of the solid surface. This is done in figure 11 which presents the droplet profiles for both geometries at time instants where this process actually takes place. The insets in this figure, zoom around the contact line area while the horizontal dashed lines indicate the baseline where the contact angles are typically evaluated. As the contact line retracts at the rear of the drop, it moves along both the upward and downward parts of the protrusions which naturally leads to

significant variations of the apparent contact angle as the droplet accommodates its shape. On the other hand, the picture is somewhat different at the advancing front because as the liquid–air interface advances it may actually touch the tip of the protrusion ahead thus creating a new contact line there. As a result, the contact line at the front actually feels only the upper part of the protrusions which leads in turn to smaller variations of the apparent advancing contact angle. The latter effect is expected to be enhanced for substrates with increasing hydrophobicity, which explains why the amplitude of the oscillations decreases with increasing values of θ_Y (see figure 10(c)) or for pillars with closer distance to each other.

3.2.3. 3D droplet on flat and patterned substrates. In order to examine the effects of substrate topography for even more realistic cases, we have also performed simulations for the case of 3D droplets. Figure 12(a) presents a simulation for a 3D droplet with $Ar = 1.413$ and $Ca = 0.202$ on a macroscopically smooth hydrophobic surface ($\theta_Y = 120^\circ$) with an inclination angle 90° . Notice that for these simulations we use different values for the disjoining pressure constants ($C_1 = 8, C_2 = 6, A = 0.038$); the local curvature at the contact line attains smaller values and is easier to resolve with coarser grids without overly affecting the solution accuracy (see also [65]). The difference between the advancing and receding contact angle is clearly shown in the side view of figure 12, while the top view of this figure shows that the droplet acquires an oval shape in line with experimental observations [9–12].

At this point we would like to make a comment regarding the relation of wettability and adhesion properties of the material, due to a misconception that is often encountered in the literature. It is well known that the increase of hydrophobicity is often accompanied by a decrease of adhesion which is typically attributed to the decrease of the contact area between the liquid and the solid. Note, however, that this is not always true. A characteristic example of such a case is the ‘rose petal effect’, where droplets wet rough surfaces with high apparent contact angles, accompanied with strong adhesion

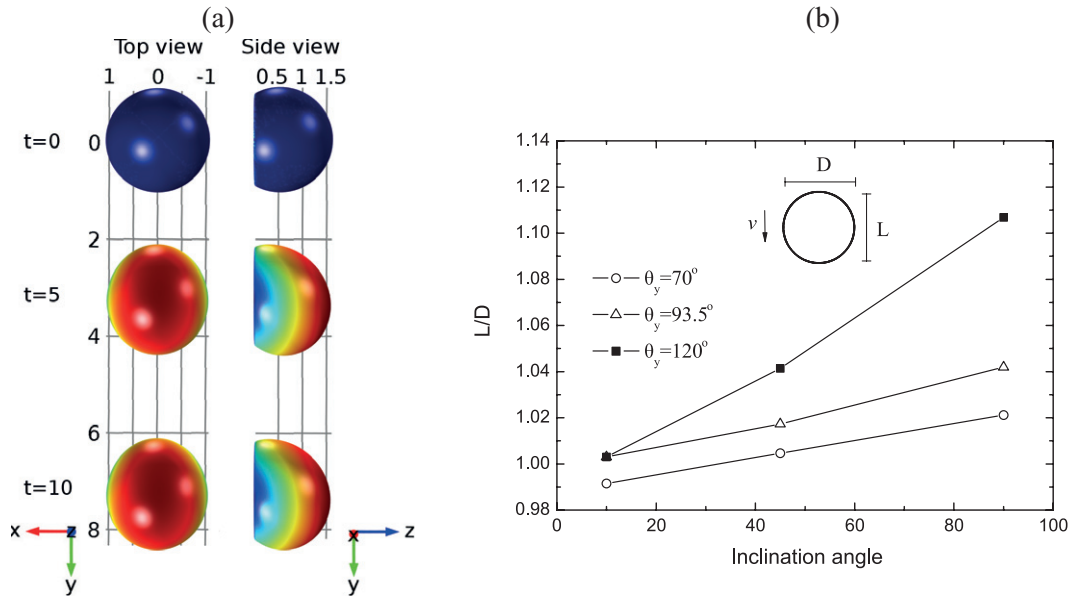


Figure 12. 3D droplet sliding on a flat inclined surface (90°). (a) Contour plot of the velocity magnitude for $\theta_Y = 120^\circ$ and (b) footprint aspect ratio as a function of θ_Y ; $Ar = 1.413$, $Ca = 0.202$, $\beta_{sl} = 10^3$, $C_1 = 8$, $C_2 = 6$, $A = 0.038$ and $\epsilon = 0.008$.

Table 2. Minimum, maximum and average values of the dynamic advancing and receding contact angles and average contact angle hysteresis for various types of substrates during $5 < t < 10$; $Ar = 1.413$, $Ca = 0.202$, $\alpha = 90^\circ$, $\theta_Y = 120^\circ$, $\beta_{sl} = 10^3$, $C_1 = 8$, $C_2 = 6$, $A = 0.038$ and $\epsilon = 0.008$.

	$\theta_{a,min}$	$\theta_{a,max}$	$\bar{\theta}_a$	$\theta_{r,min}$	$\theta_{r,max}$	$\bar{\theta}_r$	$\bar{\theta}_a - \bar{\theta}_r$
Homogeneous	126.1	126.1	126.1	113.1	113.1	113.1	13.0
Pillars	142.8	150.4	146.1	135.2	148.4	139.5	6.6
P stripes	140.2	140.3	140.3	133.9	134.2	134.0	6.3
V stripes	129.2	146.6	136.3	114.1	141.8	120.1	16.2

to the substrate [82–85]. Apparently, the adhesion properties do not depend solely on the wettability, but may also depend on the geometric configuration of the liquid–solid interface (e.g. Cassie–Baxter versus Wenzel state) and this implies that the two effects, at least macroscopically, should be examined separately. In order to examine the effect of wettability separately from the adhesion properties of the material on the dynamic hysteresis we keep constant the value of β_{sl} and plot in figure 12(b) the aspect ratio of the drop footprint for various value of θ_Y . With increasing hydrophobicity of the material the aspect ratio increases for a given inclination angle, which indicates an increase of the dynamic hysteresis. The latter behaviour may seem counter-intuitive, however, we should keep in mind that the constant value of β_{sl} implies that the adhesion properties of the material remain unchanged. The increase of the dynamic hysteresis with θ_Y may actually be attributed to the increase of the maximum height of the droplet which makes the droplet susceptible to larger deformation due to the effect of gravity.

Next we turn our attention to the case of structured substrates focusing mainly on cases where the droplet is in Cassie–Baxter state. As explained in section 2.1, in order to avoid the high computational cost, the effect of substrate topography is taken here into account through the use of equations (15) and (16) and assuming a flat solid surface. The regions of the liquid interface above the gas pockets is described by negligible

shear stress and degree of wetting ($\theta_Y = 180^\circ$) whereas in the regions where the liquid is in contact with the solid the equilibrium Young contact angle and a finite value for the slip coefficient, β_{sl} , are applied. Figure 13 depicts the footprints of a droplet sliding downwards on a surface with pillars or with stripes which are parallel or vertical to the direction of motion at $t = 10$ and for the same parameters as in figure 12. The grey areas in the figure indicate the regions where the liquid is in contact with the solid surface. As expected the shape of the outer contact line is affected significantly by the presence and geometrical characteristics of the structures. The latter also affect significantly the sliding velocity of the droplet and as it is shown in figure 13(d), the pillared surface provides less resistance to the motion of the droplet due to the decreased contact area between the liquid and the solid.

The evolution of the dynamic advancing and receding contact angles exhibits an oscillatory behaviour as the contact line moves along the asperities of the solid surface similarly to the cases of figures 8 and 10(b). The amplitude of these oscillations along with the average values of both contact angles and their difference over a large time range ($5 < t < 10$) is presented in table 2; note that the contact angles have been evaluated at the mid-plane of the drop. As it is shown, the hysteresis for the case of pillars and stripes parallel to the droplet motion decreases in comparison to the case of a homogeneous substrate. Interestingly, it is found that the effect of hysteresis

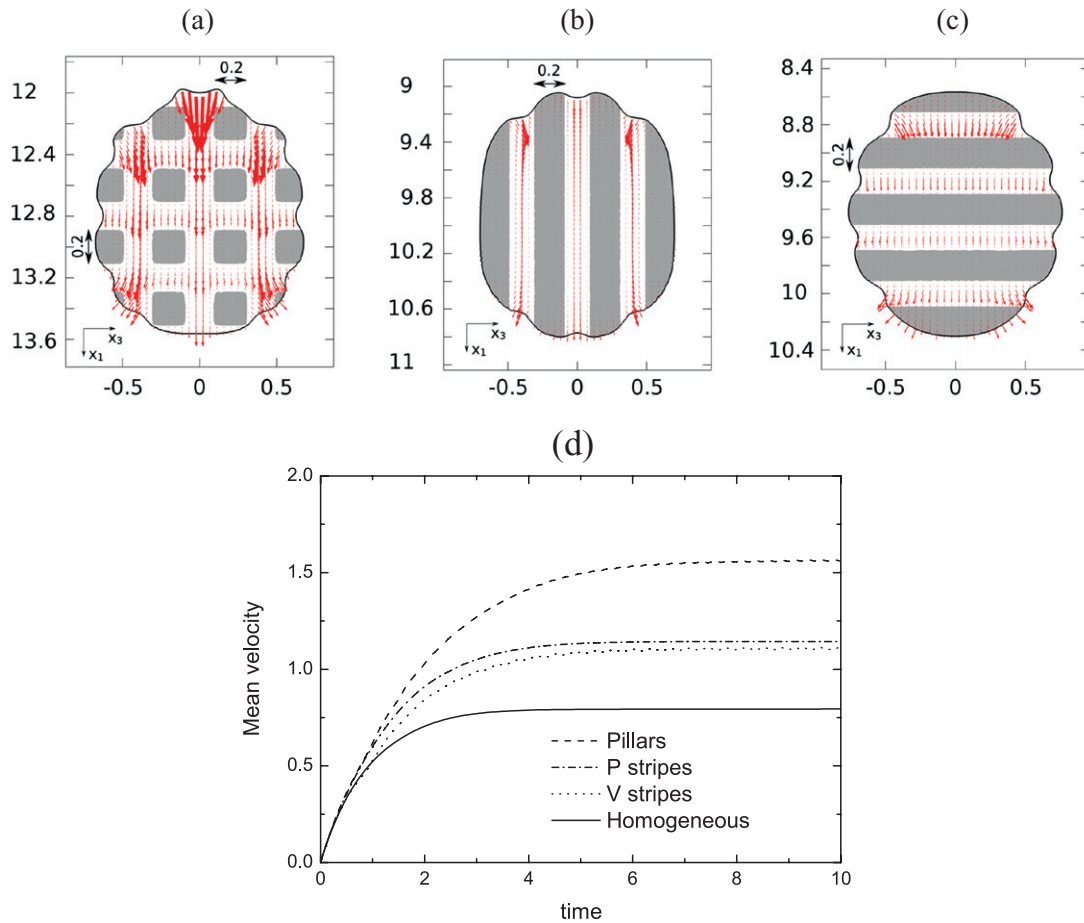


Figure 13. Footprint profiles of a 3D droplet sliding downwards on a inclined surface (90°) with (a) pillars ($\lambda_{x_1} = \lambda_{x_3} = 0.4$), (b) parallel ($\lambda_{x_1} = 0.4$) and (c) vertical ($\lambda_{x_3} = 0.4$) stripes to the direction of motion at $t = 10$. (d) Evolution of the droplet mean velocity for various types of substrates; $Ar = 1.413$, $Ca = 0.202$, $\theta_Y = 120^\circ$, $\beta_{sl} = 10^3$, $C_1 = 8$, $C_2 = 6$, $A = 0.038$ and $\epsilon = 0.008$.

increases considerably when the droplet moves vertically to the direction of the stripes, indicating that the directionality is an important factor and should be taken into account. At this point we should note that when considering a 2D droplet on a structured substrate (e.g. see the case of figure 10(b)) the flow resembles more the case of figure 13(c) and this could also provide an explanation why the predicted hysteresis in this case is significantly higher than the experimental observations.

4. Summary and conclusions

We have carried out a numerical investigation of droplets impacting or sliding on inclined complex solid surfaces. We focused on the prediction of the dynamic contact angles and the effect of static and dynamic hysteresis and how the latter depend on factors such as the inclination angle, droplet size, surface tension and topography of the substrate.

An efficient sharp-interface model has been employed, which treats the liquid–gas and liquid–solid interfaces in a unified context. The micro-scale liquid–solid interactions are taken into account through a type of Lennard–Jones potential. The robustness of this scheme is due to the fact that the dynamic contact angles emerge ‘naturally’ as a result of the

liquid–solid micro-scale interactions, capillary pressure and viscous stresses without the need of imposing an explicit condition at the contact line and without any requirement for the predefinition of the number and position of the contact lines present in the system. As it is shown, the model is particularly efficient in the case of flows with changes in the topology, e.g. in the case of an impinging droplet. In addition, the proposed modelling approach can be trivially used to examine the effect of the any kind of complex geometrical structure of the substrate (even hierarchical patterned solid surfaces) on the spreading dynamics—a difficult task for the conventional sharp-interface hydrodynamic models, because it allows the modelling of interfacial dynamics in the presence of multiple, *a priori* unknown, dynamic contact lines. It is also shown that the model has a built-in capability to predict the effect of contact angle hysteresis and especially for the case of structured solid surfaces it is possible to predict the effect of static hysteresis for a given geometry of the substrate.

Our parametric study focuses mainly on surfaces composed of hydrophobic materials. We examine the case of an impinging droplet and compare against earlier experimental observations in the literature for smooth substrates. We also examine the case of droplet impact on structured surfaces and it is shown that the final state of the droplet, i.e. whether it will

impregnate the solid structures or not, depends on the initial kinetic energy of the droplet and the aspect ratio of the solid structures, in line with earlier experimental observations. In addition, we investigate the droplet dynamics sliding on an inclined flat or structured substrate. As expected, for homogeneous and macroscopically flat solid surfaces the model predicts a finite dynamic contact angle hysteresis and no static hysteresis. Interestingly, in the case of a structured substrate the model additionally predicts the effect of static hysteresis and the droplet slides only beyond a critical inclination angle. We also examine structures which may promote the Cassie–Baxter wetting state and demonstrate that the presence of air inclusions trapped in the micro-structure of a hydrophobic substrate result in the decrease of contact angle hysteresis and in the increase of the droplet migration velocity in qualitative agreement with experimental observations for super-hydrophobic surfaces. Finally, we present 3D calculations which indicate that the directionality of the substrate topography with respect to the droplet motion may affect significantly the observed contact angle hysteresis.

Acknowledgments

The authors kindly acknowledge funding from the European Research Council under the Europeans Community's Seventh Framework Programme (FP7/2007-2013)/ERC grant agreement no. [240710] and the COST Action MP1106.

References

- [1] Kistler S F and Schweizer P M 1997 *Liquid Film Coating: Scientific Principles and Their Technological Implications* (London: Chapman and Hall)
- [2] Wijshoff H 2010 *Phys. Rep.* **491** 77–177
- [3] Pasandideh-Fard M, Aziz S D, Chandra S and Mostaghimi J 2001 *Int. J. Heat Fluid Flow* **22** 201–10
- [4] Blake T D 2006 *J. Colloid Interface Sci.* **299** 1–13
- [5] Lauga E, Brenner M and Stone H 2007 Microfluidics: the no-slip boundary condition *Springer Handbook of Experimental Fluid Mechanics* (Berlin: Springer) pp 1219–40
- [6] Bonn D, Eggers J, Indekeu J, Meunier J and Rolley E 2009 *Rev. Mod. Phys.* **81** 739–805
- [7] Ren W, Hu D and Weinan E 2010 *Phys. Fluids* **22** 102103
- [8] Sui Y, Ding H and Spelt P D 2014 *Ann. Rev. Fluid Mech.* **46** 97–119
- [9] Podgorski T, Flesselles J M and Limat L 2001 *Phys. Rev. Lett.* **87**
- [10] Le Grand N, Daerr A and Limat L 2005 *J. Fluid Mech.* **541** 293
- [11] Snoeijer J H, Rio E, Grand N L and Limat L 2005 *Phys. Fluids* **17** 072101
- [12] Puthenveetil B A, Senthilkumar V K and Hopfinger E J 2013 *J. Fluid Mech.* **726** 26–61
- [13] Savva N and Kalliadas S 2013 *J. Fluid Mech.* **725** 462–91
- [14] Spelt P D M 2005 *J. Comput. Phys.* **207** 389–404
- [15] Huang J J, Huang H and Wang X 2014 *Phys. Fluids* **26** 062101
- [16] Anderson D M and Davis S H 1995 *Phys. Fluids* **7** 248
- [17] Fang C, Hidrovo C, Wang F M, Eaton J and Goodson K 2008 *Int. J. Multiph. Flow* **34** 690–705
- [18] Dupont J B and Legendre D 2010 *J. Comput. Phys.* **229** 2453–78
- [19] Semperebon C and Brinkmann M 2014 *Soft Matter* **10** 3325–34
- [20] Schwartz L W and Eley R R 1998 *J. Colloid Interface Sci.* **202** 173–88
- [21] Schwartz L W 1998 *Langmuir* **14** 3440–53
- [22] Dupuis A and Yeomans J M 2004 *Future Gen. Comput. Syst.* **20** 993–1001
- [23] Kusumaatmaja H and Yeomans J M 2007 *Langmuir* **23** 6019–32
- [24] Savva N and Kalliadas S 2009 *Phys. Fluids* **21** 092102
- [25] Savva N, Pavliotis G A and Kalliadas S 2011 *J. Fluid Mech.* **672** 358–83
- [26] Savva N, Pavliotis G A and Kalliadas S 2011 *J. Fluid Mech.* **672** 384–410
- [27] Richard D and Quéré D 1999 *Europhys. Lett.* **48** 286
- [28] Mahadevan L and Pomeau Y 1999 *Phys. Fluids* **11** 2449–53
- [29] Quéré D 2005 *Rep. Prog. Phys.* **68** 2495–532
- [30] Bhushan B, Jung Y C and Koch K 2009 *Phil. Trans. R. Soc. A* **367** 1631–72
- [31] Šikalo S, Tropea C and Ganić E 2005 *Exp. Therm. Fluid Sci.* **29** 795–802
- [32] Yarin A L 2006 *Annu. Rev. Fluid Mech.* **38** 159–92
- [33] Bayer I S and Megaridis C M 2006 *J. Fluid Mech.* **558** 415–49
- [34] Marengo M, Antonini C, Roisman I V and Tropea C 2011 *Curr. Opin. Colloid Interface Sci.* **16** 292–302
- [35] Antonini C, Amirfazli A and Marengo M 2012 *Phys. Fluids* **24** 102104
- [36] Yeong Y H, Burton J, Loth E and Bayer I S 2014 *Langmuir* **30** 12027
- [37] Vollmer D and Butt H J 2014 *Nat. Phys.* **10** 475–6
- [38] Liu Y, Moevius L, Xu X, Qian T, Yeomans J M and Wang Z 2014 *Nat. Phys.* **10** 515–9
- [39] Antonini C, Villa F and Marengo M 2014 *Exp. Fluids* **55** 1–9
- [40] Reyssat M, Pépin A, Marty F, Chen Y and Quéré D 2006 *Europhys. Lett.* **74** 304
- [41] Jung Y C and Bhushan B 2008 *Langmuir* **24** 6262–9
- [42] Li X, Ma X and Lan Z 2010 *Langmuir* **26** 4831–8
- [43] Bhushan B and Jung Y C 2011 *Prog. Mater. Sci.* **56** 1–108
- [44] Lee J B and Lee S H 2011 *Langmuir* **27** 6565–73
- [45] Li X, Mao L and Ma X 2013 *Langmuir* **29** 1129–38
- [46] Bussmann M, Chandra S and Mostaghimi J 2000 *Phys. Fluids* **12** 3121–32
- [47] Šikalo S, Wilhelm H D, Roisman I V, Jakirlic S and Tropea C 2005 *Phys. Fluids* **17** 062103
- [48] Yokoi K, Vadillo D, Hinch J and Hutchings I 2009 *Phys. Fluids* **21** 072102
- [49] Mukherjee S and Abraham J 2007 *J. Colloid Interface Sci.* **312** 341–54
- [50] Caviezel D, Narayanan C and Lakehal D 2008 *Microfluid. Nanofluid.* **5** 469–78
- [51] Shin S and Juric D 2009 *J. Mech. Sci. Technol.* **23** 2434–43
- [52] Muradoglu M and Tasoglu S 2010 *Comput. Fluids* **39** 615–25
- [53] Eggers J, Fontelos M A, Josserand C and Zaleski S 2010 *Phys. Fluids* **22** 062101
- [54] Tanaka Y, Washio Y, Yoshino M and Hirata T 2011 *Comput. Fluids* **40** 68–78
- [55] Sprittles J E and Shikhmurzaev Y D 2012 *Phys. Fluids* **24** 082001
- [56] Ganesan S 2013 *Microfluid. Nanofluid.* **14** 615–25
- [57] Sui Y and Spelt P D M 2013 *J. Fluid Mech.* **715** 283–313
- [58] Malgarinos I, Nikolopoulos N, Marengo M, Antonini C and Gavaises M 2014 *Adv. Colloid Interface Sci.* **212** 1–20
- [59] Hyvälouma J and Timonen J 2008 *Europhys. Lett.* **83** 64002
- [60] Ellis A S, Smith F T and White A H 2011 *Q. J. Mech. Appl. Math.* **64** 107–39
- [61] Gac J M and Grado L 2012 *Colloids Surf. A: Physicochem. Eng. Asp.* **414** 259–66
- [62] Quan Y and Zhang L Z 2014 *Langmuir* **30** 11640
- [63] Chamakos N T, Kavousanakis M E and Papatthanasiou A G 2013 *Soft Matter* **9** 9624

- [64] Chamakos N T, Kavousanakis M E and Papathanasiou A G 2014 *Langmuir* **30** 4662–70
- [65] Chamakos N T, Kavousanakis M E, Boudouvis A G and Papathanasiou A G 2016 (arXiv:1601.06540)
- [66] Starov V M 2010 *Adv. Colloid Interface Sci.* **161** 139–52
- [67] Craster R V and Matar O K 2006 *J. Colloid Interface Sci.* **303** 503–16
- [68] Craster R V and Matar O K 2009 *Rev. Mod. Phys.* **81** 1131
- [69] Starov V M and Velarde M G 2009 *J. Phys.: Condens. Matter* **21** 464121
- [70] Kavousanakis M E, Chamakos N T and Papathanasiou A G 2015 *J. Phys. Chem. C* **119** 15056–66
- [71] Tucker P 2003 *J. Comput. Phys.* **190** 229–48
- [72] Karapetsas G, Matar O K, Valluri P and Sefiane K 2012 *Langmuir* **28** 11433–9
- [73] Karapetsas G and Bontozoglou V 2015 *J. Non-Newton. Fluid Mech.* **217** 1–13
- [74] Ruiter J D, Mugele F and Ende D V D 2015 *Phys. Fluids* **27** 012104
- [75] Ruiter J D, Ende D V D and Mugele F 2015 *Phys. Fluids* **27** 012105
- [76] Bartolo D, Bouamrène F, Verneuil A, Buguin A, Silberzan P and Moulinet S 2006 *Europhys. Lett.* **74** 299
- [77] Deng T, Varanasi K K, Ming H, Bhate N, Keimel C, Stein J and Blohm M 2009 *Appl. Phys. Lett.* **94** 133109
- [78] He B, Lee J and Patankar N A 2004 *Colloids Surf. A: Physicochem. Eng. Asp.* **248** 101–4
- [79] Gauthier E, Hellstern T, Kevrekidis I G and Benziger J 2012 *ACS Appl. Mater. Interfaces* **4** 761–71
- [80] Reyssat M, Richard D, Clanet C and Quéré D 2010 *Faraday Discuss.* **146** 19–33
- [81] Marmor A 2011 *Eur. Phys. J. Spec. Top.* **197** 193–8
- [82] Feng L, Zhang Y, Xi J, Zhu Y, Wang N, Xia F and Jiang L 2008 *Langmuir* **24** 4114–9
- [83] Bormashenko E, Stein T, Pogreb R and Aurbach D 2009 *J. Phys. Chem. C* **113** 5568–72
- [84] Bhushan B and Nosonovsky M 2010 *Phil. Trans. R. Soc. A* **368** 4713–28
- [85] Bormashenko E 2015 *Adv. Colloid Interface Sci.* **222** 92–103